Journal of
Applied Remote Sensing

RemoteSensing.SPIEDigitalLibrary.org

Development and characterization of Carbon Observing Satellite

Hang Zhang
Chao Lin
Yuquan Zheng
Wenquan Wang
Longfei Tian
Dongbin Liu
Shuai Li

SPIE.

Hang Zhang, Chao Lin, Yuquan Zheng, Wenquan Wang, Longfei Tian, Dongbin Liu, Shuai Li, "Development and characterization of Carbon Observing Satellite," *J. Appl. Remote Sens.* **10**(2), 024003 (2016), doi: 10.1117/1.JRS.10.024003.

Development and characterization of Carbon Observing Satellite

Hang Zhang,[a,b] Chao Lin,[b] Yuquan Zheng,[b] Wenquan Wang,[a,*] Longfei Tian,[c] Dongbin Liu,[b] and Shuai Li[b]

[a]Jilin University, College of Physics, No. 2699 Qianjin Road, Changchun 130012, China
[b]Changchun Institute of Optics, Fine Mechanics and Physics,
Chinese Academy of Sciences, No. 3888 Dong Nanhu Road, Changchun 130033, China
[c]Shanghai Engineering Center for Microsatellites, No. 99 Haike Road, Shanghai 201203, China

Abstract. Carbon Observing Satellite (Tan-Sat) is the first satellite of China designed to monitor column-averaged atmospheric carbon dioxide (X_{CO2}) by detecting gas absorption spectra of the solar shortwave infrared radiation reflected from the Earth's surface and atmosphere. Two instruments are accommodated on Tan-Sat: the high resolution hyperspectral sensor for carbon observation grating spectrometer (HRHS-GS) and the cloud and aerosol polarimetric imager (CAPI). HRHS-GS will provide the space-based measurements of CO_2 on a scale and with the accuracy and precision to quantify terrestrial sources and sinks of CO_2. CAPI is used to identify the contamination by optically thick clouds and to minimize the impact of scattering by aerosol. These two instruments work together to collect global column CO_2 concentrations with correction for cloud and aerosol contamination. The instrument design of HRHS-GS is presented. Ocean reflectivity and the incident radiation of the instrument for transverse electric and transverse magnetic polarizations in glint mode are discussed. The changes to glint mode operation are described. The spectral characteristics of HRHS-GS were determined through the laser-based spectral calibration. The onboard spectral calibration method based on spectrum matching is introduced. The availability was verified, satisfying the onboard spectral calibration accuracy requirement of better than $\Delta\lambda/10$ ($\Delta\lambda$ is spectral resolution). © *2016 Society of Photo-Optical Instrumentation Engineers (SPIE)* [DOI: 10.1117/1.JRS.10.024003]

Keywords: carbon dioxide; Carbon Observing Satellite; optical design; polarization; spectral calibration; spectrum matching.

Paper 15494 received Aug. 6, 2015; accepted for publication Apr. 27, 2016; published online May 27, 2016.

1 Introduction

The global warming issue has attracted the general attention of every country in the world on increasing emission of greenhouse gases (GHGs). Human activities, including fossil fuel extraction and combustion, land use practices, emit large amounts of GHGs into the atmosphere. Among the most important GHGs are CO_2 and methane (CH_4). Atmospheric CO_2 concentrations have increased by almost 40% since preindustrial times, from ~280 parts per million by volume (ppmv) in the 18th century to 390 ppmv in 2010. The current CO_2 level is higher than it has been in at least 800,000 years.[1] In view of the significant influence of CO_2, countries around the world have developed a variety of methods to monitor this gas using remote sensing observations from space and have launched many optical remote sensing monitoring instruments.[2,3] In terms of the National Medium and Long-term Science and Technology Development Plan (2006 to 2020)[4] and China's National Climate Change Programme,[5] an important project, "the Global Carbon Dioxide Monitoring Scientific Experimental Satellite Demonstration," is set in the field of Earth observation by the National High Technology Research and Development Program of China (863 Program), aiming at providing data for carrying out global climate change research.[6]

*Address all correspondence to: Wenquan Wang, E-mail: panni0119_cn@sina.com; wangwq@jlu.edu.cn

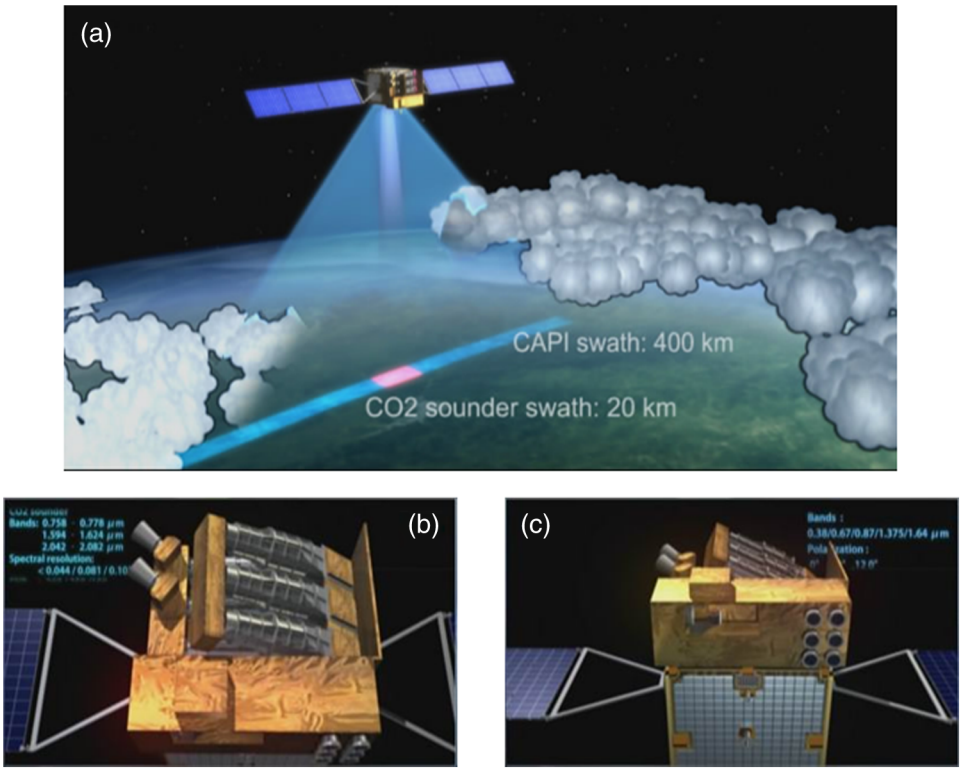

Fig. 1 Artist conception of Tan-Sat. (a) HRHS-GS swath is 20 km and CAPI swath is 400 km. CAPI has continuous spatial coverage swath and higher spatial resolution than HRHS-GS in order to detect the aerosol spatial distribution and cloud coverage. (b) The outer structure of HRHS-GS. (c) The outer structure of CAPI.

The project implements an experimental scientific satellite for monitoring CO_2 globally with high spatial and spectral resolution. The project also implements a data processing and verification system that can resolve variations in the CO_2 concentration monitoring as 1% (4 ppm out of the ambient 400 ppm background) in China and other key areas.

Carbon Observing Satellite (Tan-Sat) is the first experimental scientific satellite produced by China for monitoring the column densities of CO_2 in the atmosphere. Tan-Sat is scheduled to be launched in July 2016. It will be placed in a sun-synchronous orbit at the height of about 700 km on $13:30 \pm 30$ min local time, with an inclination angle of 98.75 deg. The lifetime of Tan-Sat is designed for 3 years. It carries two key instruments, high resolution hyperspectral sensor for carbon observation grating spectrometer (HRHS-GS) and cloud and aerosol polarimetric imager (CAPI),[7,8] as shown in Fig. 1. The function of HRHS-GS is to obtain CO_2 and oxygen by measuring their absorption spectrum. The main purposes of CAPI are to identify cloud contamination and to characterize optical path length uncertainties associated with scattering by clouds and aerosols.[9–11]

This paper is organized as follows: Sec. 2 provides a brief description of HRHS-GS, including the main characteristics, the optical design, and the detectors of HRHS-GS. Section 3 describes polarization observation of the instrument in glint mode over ocean. The laboratory and on-orbit spectral calibration are described in Sec. 4. A summary of this paper and follow-up plans are given in Sec. 5.

2 Design of High Resolution Hyperspectral Sensor for Carbon Observation Grating Spectrometer

2.1 *Overview*

HRHS-GS employs large area diffraction grating spectrometers and uses a pointing mirror in conjunction with the satellite platform to collect observations in nadir, glint, and target

modes[12,13] (Fig. 2). The optical system has been designed with high spectral resolution and high signal to noise to yield high sensitivity, even over low-albedo surfaces. With the high-precision CO_2 metrical data, relative retrieval accuracy of CO_2 column amount is 1 to 4 ppm.[14–16]

HRHS-GS, the main payload of Tan-Sat, has three spectral bands, which cover narrow spectral ranges in the visible and near-infrared (VNIR) and shortwave infrared (SWIR). The instrument is a push broom imaging system using a two-dimensional (2-D) focal plane array (FPA) detector. The main specifications of HRHS-GS are summarized in Table 1.

2.2 *Optical Design of High Resolution Hyperspectral Sensor for Carbon Observation Grating Spectrometer*

The optical system of HRHS-GS is designed for high spectral resolution and low stray/scattered.[17,18] Figure 3 illustrates the optical layout of HRHS-GS. It consists of a pointing mirror, an afocal system (a system without focus) with double off-axis parabolic mirrors, a dichotic splitter, a focusing system, an entrance slit, a collimating system, a large-area plane diffraction grating, and a spectral imaging system.[19] The key components of the tri-channel grating spectrometer are the diffraction gratings. Each grating is 140 mm × 190 mm and the diffractive efficiency can be over 90% [in the Transverse Magnetic (TM) polarization]. Each channel in the tri-channel grating spectrometer has the same mechanics, and three gratings have the same deviation angle to ensure the high mechanic stability. The three spectral bands are coupled to a common fore optics, as shown in Fig. 4. To eliminate chromatic aberration and suppress stray/scattered light, an afocal all-reflective optical system with an intermediate focus is designed as the fore optics. A slit-shaped field stop is placed at the intermediate focus, to adjust three spectral bands and to suppress stray/scattered light.[20,21]

The beam diameter is reduced to two-thirds of the pupil size after traversing the afocal system, effectively reducing the size of the optical elements that follow. The three spectral bands are separated by the spectral relay system and isolated by dichroic beam splitters. The three beams of light pass through, respectively, a narrow bandpass filter to generate narrow band parallel light with the wavelength range of the three spectral bands. Each channel is focused onto the entrance slit. A linear polarizer placed in front of the entrance slit is used to select the polarization vector perpendicular to the long axis of the slit (only the TM-polarized light can enter the spectrometer) and to suppress the zero order stray light of the spectrometer. The light via the entrance slit is collimated by two pieces of quartz lens and diffracted by the diffraction grating. Then, the first-order diffraction light of the diffraction grating passes through the other two pieces of quartz lens and images on a 2-D FPA, thereby obtaining fine absorption information on the atmosphere.[22]

By setting a zero order light trap and other stray light removal methods, the stray light in the system can decrease to 10^{-5}, and its spatial modulation transfer function is more than 0.9 (at 1.4 lp/mm), and the spectral resolution of the spectrometer exceeds 0.035 nm (at 760 nm).

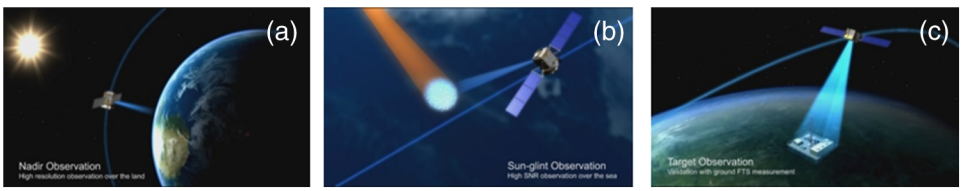

Fig. 2 HRHS-GS observation modes. (a) Nadir mode. In nadir mode, the attitude control system (ACS) points the instrument aperture to the local nadir, so that data can be collected along the ground track just below the spacecraft. (b) Glint mode. In glint mode, the ACS is programmed to point the instrument aperture between the local nadir the bright "glint" spot, where sunlight is specularly reflected from the Earth's surface. (c) Target mode. In target mode, the ACS points the instrument aperture at specific stationary surface targets as the satellite flies overhead.

Table 1 Main specification of HRHS-GS.

Parameters	Band1 (O_2 A-band)	Band2 (weak CO_2 band)	Band3 (strong CO_2 band)
Central wavelength (nm)	760	1610	2060
Spectral range (nm)	758 to 778	1594 to 1624	2041 to 2081
Spectral resolution $\Delta\lambda$ (nm)	0.033 to 0.047	0.12 to 0.138	0.16 to 0.182
Spectral sampling	2.0 to 2.8 pixels per slit	2.0 to 2.3 pixels per slit	2.0 to 2.7 pixels per slit
Pupil diameter (mm)		140	
Focal length (mm)		252	
Focal ratio		1.8	
Signal-to-noise ratio	$\geq$350:1 at 5.8×10^{19} photons/s/m^2/sr/μm	$\geq$250:1 at 2.1×10^{19} photons/s/m^2/sr/μm	$\geq$180:1 at 1.1×10^{19} photons/s/m^2/sr/μm
Integration time		0.293 s	
Data depth (bits)		14	
Pointing mirror		Pointing range: -30 to $+10$ deg	
		Pointing precision: better than $\pm1.5'$	
		Measuring precision: better than 30''	
Observation modes		Nadir; target; sun-glint; occultation	
Ground sample distance (at 700 km)		2 km $\times$ 2 km	
Swath (km)		$\geq$20	
Calibration		Precision: 4.6% (absolute); 2.55% (relative)	
		Calibration period: 1 day	
Resistant irradiation (total dose)		> 10 krad (Si)	
Power dissipation		Standby mode: <120 W	
		Work mode: <220 W	
		Safe mode: <40 W	
Weight (kg)		$<202\pm1.8$	

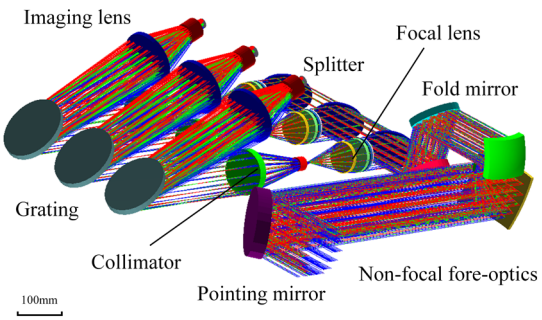

Fig. 3 Optical layout of HRHS-GS.

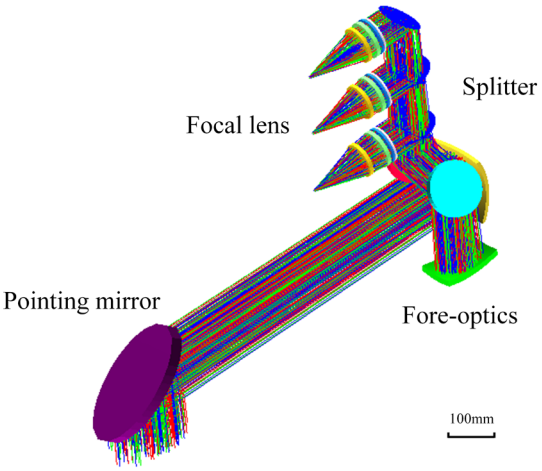

Fig. 4 Layout of fore optics.

2.3 *Detectors of High-Resolution Hyperspectral Sensor for Carbon Observation Grating Spectrometer*

The three gratings disperse light of different spectral ranges onto the FPAs in the direction orthogonal to the long dimension of the entrance slit. There is an area array detector at the focus of each channel of the spectrometer to record the spectrum. One dimension measures the different spectra while the other one measures field angles along the entrance slit.

For the O_2 A-band in the spectral range from 758 to 778 nm, the spectral resolution is 0.04 nm and the ground resolution is 2×2 km with a 20-km swath. To meet mission requirement, the silicon detector E2V55-30[23] is chosen for the O_2 A-band channel, as shown in Fig. 6(a). The detector E2V55-30 is manufactured by E2V Technologies (United Kingdom). Standard three-phase clocking and buried channel charge transfer are employed. The detector has excellent antiblooming, low dark current, and high dynamic range. The large pixel and the ability to bin images are features that are well suited to spectrum detection. It operates in a frame transfer mode with a store shield. The detector is 1252×1152 pixel arrays with 22.5 μm $\times$ 22.5 μm pixels, it is split into a top section A and a bottom section B, and each section has 1252×576 pixels. The section A is defined to image area, and the section B is defined to store area with a store shield. The section C is used for horizontal readout of pixels. Figure 5 illustrates the architecture of the detector E2V55-30. About 320 pixels are used out of the 576 in the spatial dimension parallel to the entrance slit, in order to improve the signal-to-noise

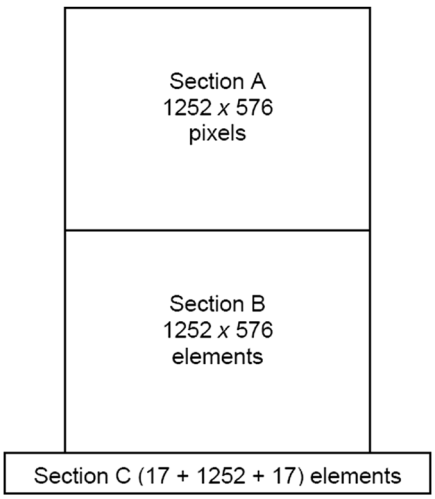

Fig. 5 Architecture of the detector E2V55-30.

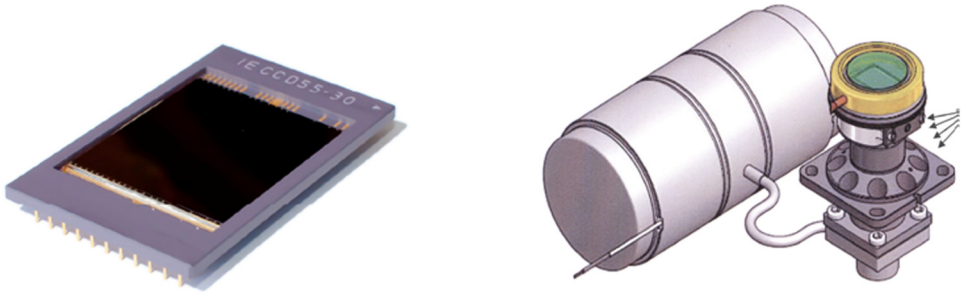

Fig. 6 Detectors: (a) silicon detector E2V55-30 for the O_2 A-band, and (b) HgCdTe detector SATURN SW LSF for the weak CO_2 and the strong CO_2 band.

ratio (SNR), 16 adjacent pixels are merged to produce up 20 spatially averaged "super pixels."[13] Spectral dimension has 1252 pixels and 5 pixels are blocked out on each side of the array. About 1200 pixels are used (means 1200 spectral channels in the O_2 A-band), and different wavelengths correspond to different pixel position along the spectral dimension. Due to little dark signal (65 e/pixel/second at 273 K), the O_2 A-band detector does not need a cooler.

The detectors in the two CO_2 channels use mercury cadmium telluride (HgCdTe) as the photosensitive material. The detector SATURN SW LSF[24] from Sofradir Company is chosen for 1.61 and 2.06-μm band, as shown in Fig. 6(b). It consists of a 500×240 pixels array, with a pixel pitch of 30 μm. The detector array operates in full staring mode with simultaneous integration of charges during readout of a previous frame. Similar to the O_2 A-band, 240 pixels of spatial dimension are binned to 20 pixels for better SNR. Because the dark noise of HgCdTe detectors increases with rising temperature, a Stirling cryocooler is used to maintain the HgCdTe detectors at their operating temperature (150 K).

3 Polarization of the Instrument

Orbiting Carbon Observatory-2 (OCO-2) is the first NASA satellite designed to measure atmospheric CO_2 with the accuracy, resolution, and coverage needed to detect CO_2 sources and sinks on regional scales over the global.[3] It was launched on July 2, 2014. Based on the observed data of 20 days, the statistical analysis of effective observation points for X_{CO2} retrievals is made, as shown in Fig. 7.

As can be seen in Fig. 7, effective observation points of OCO-2 for X_{CO2} retrievals in Nadir mode mainly concentrate on land areas; in glint mode, more effective observation points can be acquired on both ocean and land areas. For efficient data utilization, glint observations have more important significance for global X_{CO2} retrievals.

By comparing between theoretical simulation and onboard data of OCO-2, the relationship between polarization state and incident signal of the instrument for glint observations is given.

In radiative transfer process, energy loss of sunlight is related to Earth's surface (ocean or land) reflectivity, atmospheric attenuation, and cloud and aerosol scattering. In the actual retrievals, the data contaminated seriously by cloud and aerosol will be rejected; therefore, cloud and aerosol interference does not need to be considered. Atmospheric attenuation changes with the solar incident angles (the solar zenith angles), resulting in variation of incident radiation intensity of the instrument. Radiative transfer process is shown in Fig. 8.

Transmissivity of incident process can be expressed as

$$T_{\text{in}} = \exp(-\tau_{\text{in}}) = \exp\left[-\frac{\tau}{\cos(\theta_{\text{sza}})}\right]. \tag{1}$$

Transmittance of emergent process can be expressed as

$$T_{\text{out}} = \exp(-\tau_{\text{out}}) = \exp\left[-\frac{\tau}{\cos(\theta_{\text{vza}})}\right]. \tag{2}$$

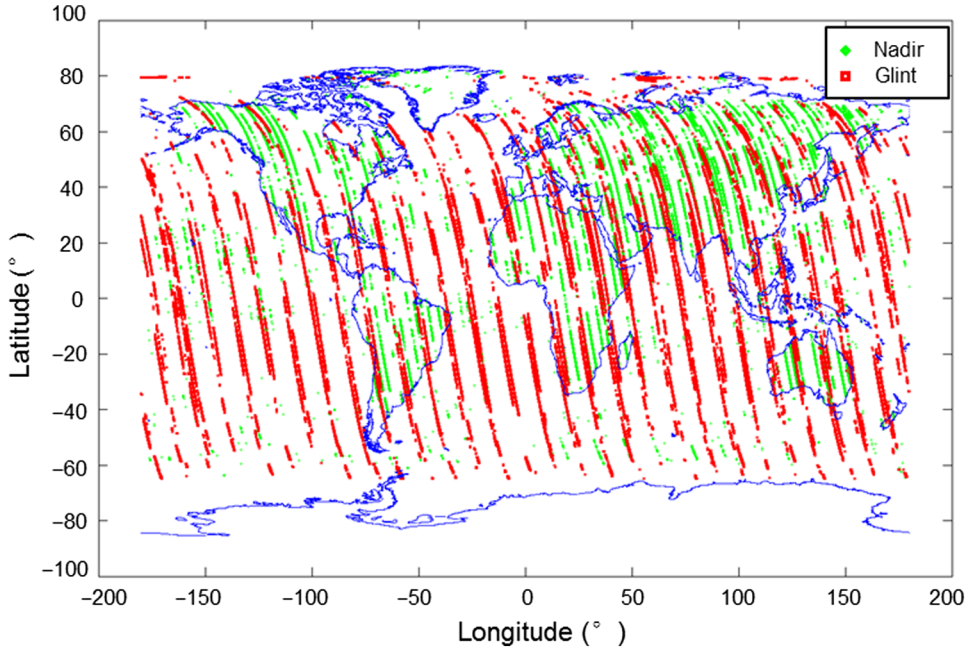

Fig. 7 Effective observation points of OCO-2 for X_{CO2} retrievals. The green diamonds represent effective observation points for nadir observation and the red squares represent effective observation points for glint observations.

The sunlight traverses the atmosphere and is reflected by the Earth's surface, emergent radiation at the top of the atmosphere, which can be received by the instrument:

$$R_{\text{out}} = R_0 \cdot T_{\text{in}} \cdot r \cdot T_{\text{out}} = R_0 \cdot \exp\left[-\frac{\tau}{\cos(\theta_{\text{sza}})}\right] \cdot r \cdot \exp\left[-\frac{\tau}{\cos(\theta_{\text{vza}})}\right]. \tag{3}$$

When $\theta_{\text{sza}} = \theta_{\text{vza}}$, glint observations achieve best effect, $T_{\text{in}} = T_{\text{out}}$, emergent radiation at the top of the atmosphere is

$$R_{\text{out}} = R_0 \cdot \left\{\exp\left[-\frac{\tau}{\cos(\theta_{\text{sza}})}\right]\right\}^2 \cdot r. \tag{4}$$

The reflectivity of TM polarization is significantly different from the one of transverse electric (TE) polarization. According to Fresnel equations, the reflectivity of the two polarization states can be expressed as

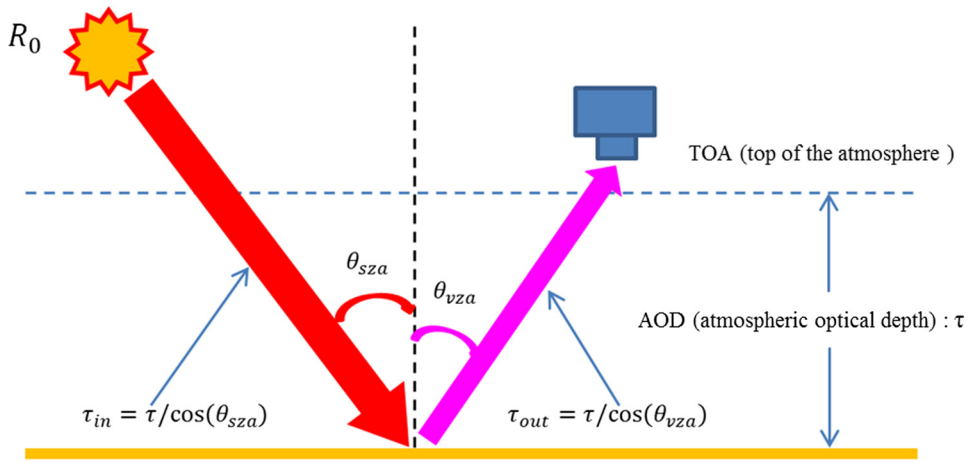

Fig. 8 Radiative transfer process in glint mode. θ_{sza} is the angle of incidence (the solar zenith angle), θ_{vza} is the angle of reflection, τ is atmospheric optical depth (AOD).

$$r_{\mathrm{TE}} = \frac{\sin^2(i_1 - i_2)}{\sin^2(i_1 + i_2)}, \tag{5}$$

$$r_{\mathrm{TM}} = \frac{\tan^2(i_1 - i_2)}{\tan^2(i_1 + i_2)}, \tag{6}$$

where i_1 is the angle of incidence and i_2 is the angle of refraction. i_2 can be determined according to $n_1 \sin i_1 = n_2 \sin i_2$, $n_1 = 1$ for air and $n_2 = 1.34$ for seawater. The relationship between the reflectivity of the two polarization states and the solar zenith angle for glint observations is shown in Fig. 9.

For original design of the satellite attitude, the polarization axis of HRHS-GS was TM polarization (HRHS-GS was only sensitive to light that was polarized in the direction perpendicular to the long axis of the slit). As shown in Fig. 9, there was only TE-polarized light in the reflected light of seawater over the ocean near the Brewster angle (~53 deg for seawater). The polarization axis of HRHS-GS was perpendicular to the polarization state of the incident light of HRHS-GS. Only diffuse reflection light of seawater entered the instrument, the incident signal was too weak for data retrievals. The SNR of the instrument is mainly related to two elements, one is the performance of the instrument (such as detector noise, diffraction efficiency of the grating, parameters of optical system), and the other is the incident radiation intensity of the instrument. Therefore, the polarization influences the SNR of the instrument, and then influences the precision of X_{CO2} retrievals.

OCO-2 also encountered the same problem, its original plan was to maintain the long axis of the slit perpendicular to the "principal plane," but this viewing geometry provided too little signal over the ocean near the Brewster angle.[25] In order to solve this problem, the OCO-2 was rotated 30 deg around the telescope optical axis to increase the signal for glint observations. Figure 10 shows the relationship between incident energy ratio and the solar zenith angle by simulation. It is consistent with the measured incident energy of OCO-2 on-orbit.

The emergent radiation intensity at the top of the atmosphere is very high for glint observations, even though only 25% of TE-polarized signal can enter the OCO-2 near the Brewster angle, enough SNR can be achieved for retrieval accuracy of 0.5 ppm at solar zenith angles <70 deg.[25]

Similar to OCO-2, Tan-Sat was rotated around the telescope optical axis to change the polarization axis for glint observations. As noted above, SNR of the instrument is related to the incident radiation intensity and the performance of the instrument. The performance of HRHS-GS and OCO-2 is compared in Table 2.

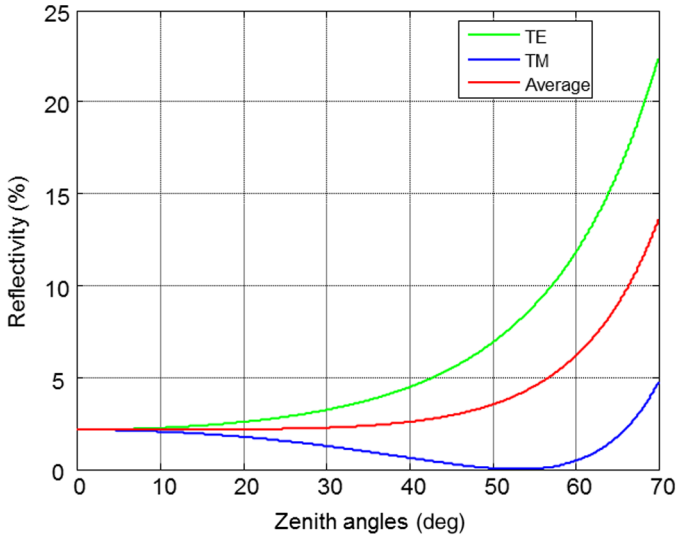

Fig. 9 The relationship between the reflectivity of the two polarization states and the solar zenith angle for glint observations. The green solid line represents TE-polarized reflectivity that was fitted based on Eq. (5); the blue solid line represents TM-polarized reflectivity that was fitted based on Eq. (6); the red solid line represents the average value of two kinds of reflectivity.

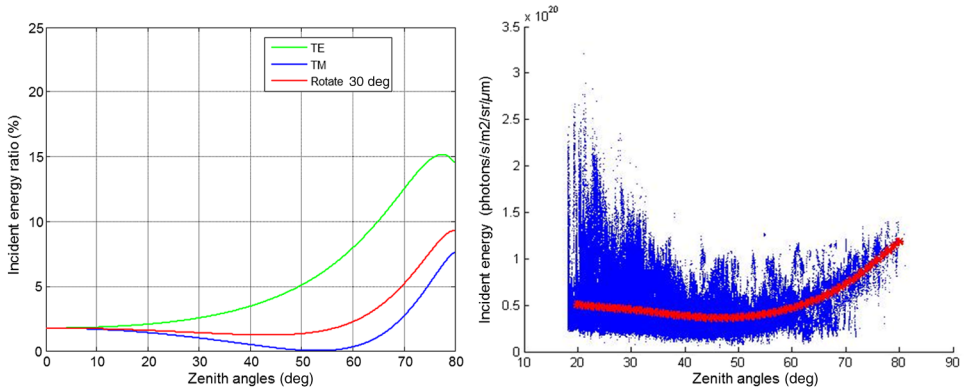

Fig. 10 Incident signal of the instrument increased for glint observations, because the OCO-2 was rotated 30 deg around the telescope optical axis. (a) Red solid line represents the relationship between incident energy ratio (the ratio of incident radiation of the instrument to the solar radiation) and the solar zenith angle by simulation (taking atmospheric attenuation into account). (b) Measured incident energy of OCO-2 on-orbit, blue spots represent the scatter diagram, red solid line is the fitted curve. Measured curve and simulated curve have the same trend of variation.

According to SNR equation:

$$\mathrm{SNR} = \frac{S_e(\lambda)}{\sqrt{N_e^2 + D_K + S_e(\lambda)}}, \tag{7}$$

where $S_e(\lambda)$ is the signal output of the detector, N_e is the readout noise, and D_K is the dark current. The SNR levels of HRHS-GS were simulated for different angles of rotation, as shown in Fig. 11.

Table 2 Comparison of the performance between HRHS-GS and OCO-2.

Parameters	HRHS-GS	OCO-2
Focal ratio	1.8	1.8
Spectral resolution (FWHM of ILS)	0.033 to 0.047 nm at 0.76 μm	0.04 nm at 0.76 μm
	0.12 to 0.142 nm at 1.61 μm	0.08 nm at 1.61 μm
	0.16 to 0.182 nm at 2.06 μm	0.1 nm at 2.06 μm
Pixel pitch	22.5 μm $\times$ 22.5 μm at 0.76 μm	18 μm $\times$ 18 μm at 0.76 μm
	30 μm $\times$ 30 μm at 1.61 μm	18 μm $\times$ 18 μm at 1.61 μm
	30 μm $\times$ 30 μm at 2.06 μm	18 μm $\times$ 18 μm at 1.61 μm
Pixel number	1242 $\times$ 576 at 0.76 μm	1024 $\times$ 1024 at 0.76 μm
	500 $\times$ 256 at 1.61 μm	1024 $\times$ 1024 at 1.61 μm
	500 $\times$ 256 at 2.06 μm	1024 $\times$ 1024 at 2.06 μm
Exposure time	0.293 s	0.333 s
Readout noise	9e- at 0.76 μm	
	250e- at 1.61 μm	20e-
	250e- at 2.06 μm	

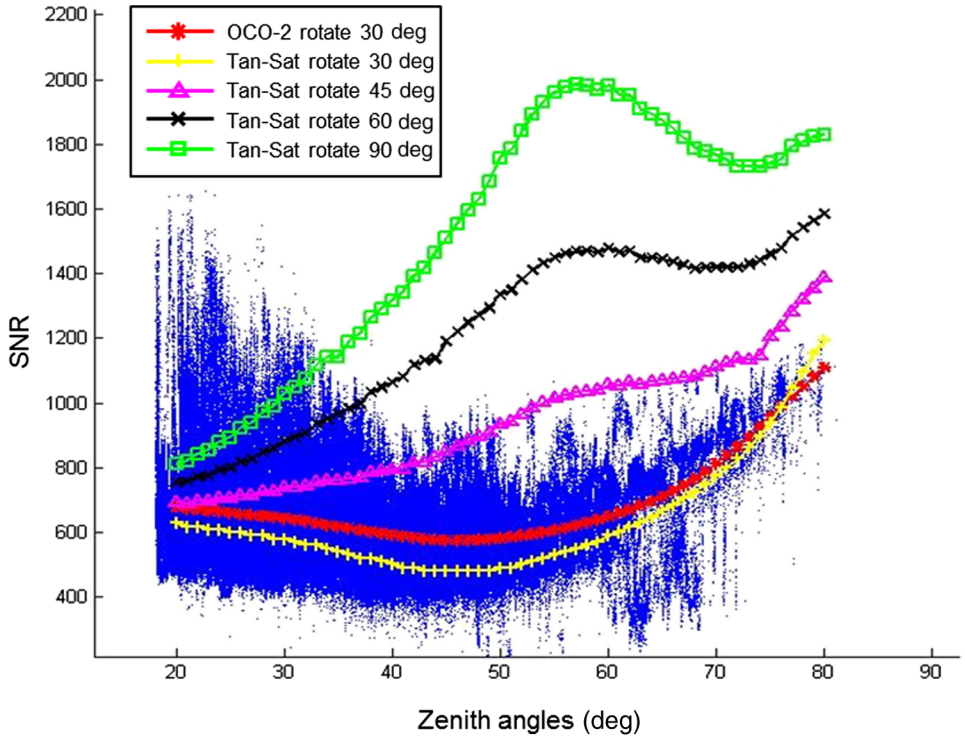

Fig. 11 The estimated SNR levels of HRHS-GS for different angles of rotation. Yellow line, pink line, black line, and green line, respectively, represent rotation angle of 30, 45, 60, and 90 deg. As a contrast, blue spots represent the scatter diagram of measured SNR of OCO-2 on-orbit, and red solid line is the fitted curve.

Here, Fig. 11 shows only the variation trend of the SNR levels of HRHS-GS for different angles of rotation, it cannot truly reflect the comparison of the on-orbit SNR levels between HRHS-GS and OCO-2. Taking into account the satellite attitude control, Tan-Sat will be rotated 45 deg around the telescope optical axis for glint observations.

4 Spectral Calibration

4.1 *Laser-Based Spectral Calibration*

The laboratory spectral calibration of HRHS-GS was used to determine the instrument line shape (ILS) function, center wavelength, and spectral resolution. The ILS profiles were derived from the tunable diode-laser testing.[26–28] For three different spectral bands, three models of tunable diode-laser from the New Focus Company were adopted. The index parameters are summarized in Table 3.

Table 3 The parameters of the tunable diode lasers.

Parameters	TLB6172 SN:0084 for 0.76-μm band	TLB6730 SN:0082 for 1.61-μm band	TLB6736 SN:0302 for 2.06-μm band
Wavelength scan range	758 to 778 nm	1550 to 1630 nm	1975 to 2075 nm
Minimum power	5 mW	4 mW	2 mW
Linewidth	<300 kHz	<300 kHz	<300 kHz
Adjustment range	0.24 nm	0.3 nm	0.3 nm
Wavelength stability	Better than 0.005 nm	Better than 0.01 nm	Better than 0.02 nm

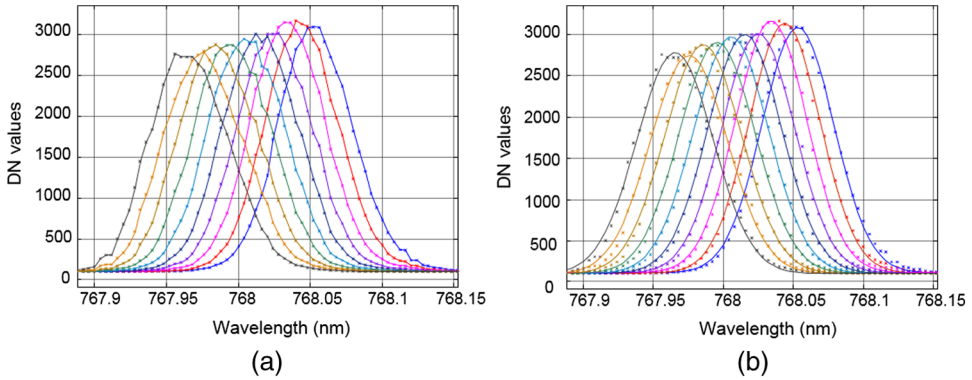

Fig. 12 Spectral pixels: (a) ILSs of the 10 spectral pixels of the 0.76-μm band, (b) Gaussian fits to ILSs of the 10 spectral pixels.

HRHS-GS was placed in the thermal-vacuum chamber at a pressure of <1 Pa and at a temperature of 253 K. Each laser was fiber coupled to two parts, one was a wavemeter for wavelength monitoring and the other was an integrating sphere as the light source. The integrating sphere was located at the focus of a collimator to output monochromatic collimated beam. The monochromatic collimated light passed into the vacuum chamber to uniformly illuminate the entrance telescope of HRHS-GS. The light traversed the slit of the spectrometer; it was collimated by a two-element collimator, dispersed by a diffraction grating. The dispersed light was then focused by imaging lens onto a 2-D FPA.

The tunable diode-laser continuously output the single-frequency light at the regular interval, scanning the entire spectral range of each band. The DN values of each pixel were recorded as spectral response for the monochromatic light. After power correction and normalization, the ILS of each spectral pixel was obtained.[29,30] The center wavelength and full-width at half-maximum (FWHM) of each spectral pixel were determined with a Gaussian fit. Figure 12 shows the ILSs of 10 pixels of the 0.76-μm band from the laser scans and the Gaussian fits to ILSs.

Laser scanning intervals were 0.005 nm, 0.01 nm, and 0.02 nm for the 0.76 μm band, 1.61 μm band and 2.06 μm band, respectively. Scan range for a signal pixel was greater than ± 3 FWHM. Due to the heavy workload of scanning the entire spectral range, one specific system was designed to automatically adjust the output wavelength of the laser according to predetermined steps, and then waiting tens of seconds for wavelength and intensity stabilization. Quick-look software would automatically store and average 50 frames of data. The wavemeter measured the stability and accuracy of laser power and wavelength in real time, the accuracy is better than 10^{-4} nm. Spectral characterization of each pixel for three bands was determined using the diode-laser method. The laser-based spectral calibration system is shown in Fig. 13.

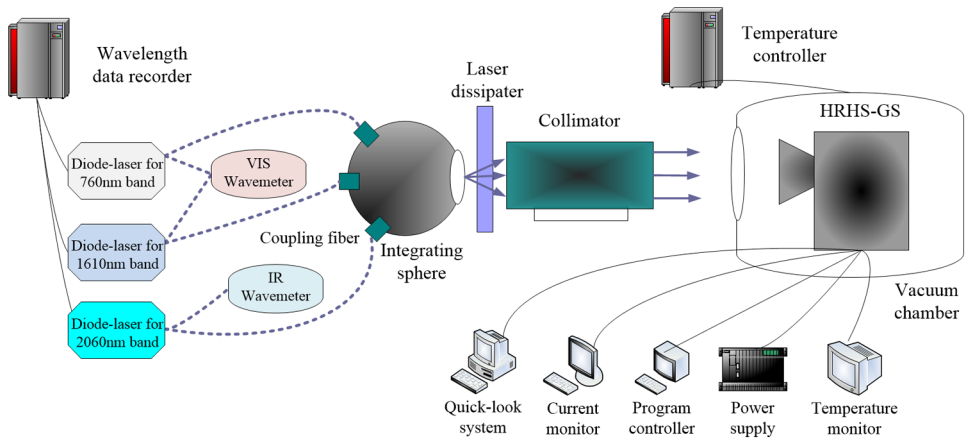

Fig. 13 The laser-based spectral calibration system scheme.

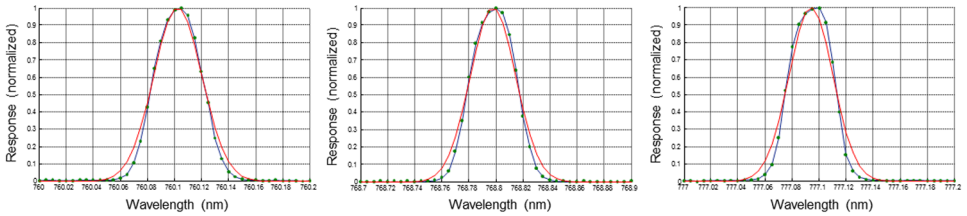

Fig. 14 Spectral response function (ILS) of several different channels on three spatial positions for the 0.76-μm band (FOV represents spatial pixel and channel represents spectral pixel): (a) FOV = 3, channel = 153, FWHM = 0.0401 nm, center wavelength = 760.103 nm; (b) FOV = 10, channel = 642, FWHM = 0.0398 nm, center wavelength = 768.798 nm; (c) FOV = 17, channel = 1181, FWHM = 0.0393 nm, center wavelength = 777.094 nm.

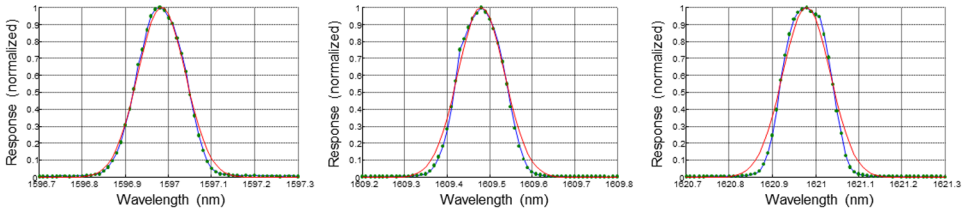

Fig. 15 Spectral response function (ILS) of several different channels on three spatial positions for the 1.61-μm band (FOV represents spatial pixel and channel represents spectral pixel): (a) FOV = 3, channel = 58, FWHM = 0.1330 nm, center wavelength = 1596.983 nm; (b) FOV = 10, channel = 258, FWHM = 0.1279 nm, center wavelength = 1609.476 nm; (c) FOV = 17, channel = 468, FWHM = 0.1307 nm, center wavelength = 1620.968 nm.

For 1 km × 2 km ground resolution, 16 spatial pixels were merged to produce up to 20 spatially averaged "super pixels." The ILS profiles of different field of views and different spectral channels are shown in Figs. 14–16.[31]

Taking the 0.76-μm O_2 A-band as an example, the results of the laboratory spectral calibration are discussed below. We scanned the entire spectral range with the tunable diode-laser at 0.005-nm intervals. The ILS and center wavelength of each spectral pixel were determined. Figure 17 shows spectral sampling, spectral resolution, and center wavelength as a function of spectral pixel index for the 0.76-μm O_2 A-band.

For mechanical dimension reason, the angle between the incident light axis and the diffraction grating is 47.282 deg. The grating disperses the spectrum onto 1200 FPA spectral columns in the direction perpendicular to the long axis of the slit. The FWHM of the slit image on the FPA is

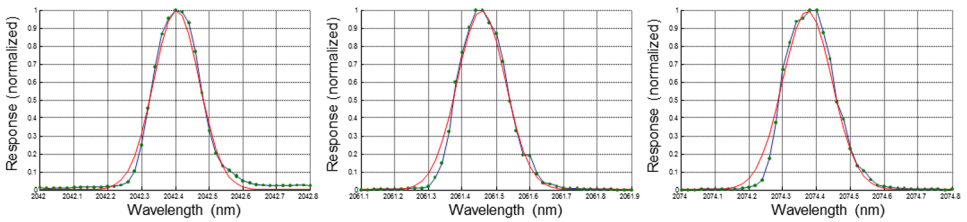

Fig. 16 Spectral response function (ILS) of several different channels on three spatial positions for the 2.06-μm band (FOV represents spatial pixel and channel represents spectral pixel): (a) FOV = 3, channel = 23, FWHM = 0.1749 nm, center wavelength = 2042.404 nm; (b) FOV = 10, channel = 259, FWHM = 0.1721 nm, center wavelength = 2061.455 nm; (c) FOV = 17, channel = 431, FWHM = 0.1723 nm, center wavelength = 2074.373 nm.

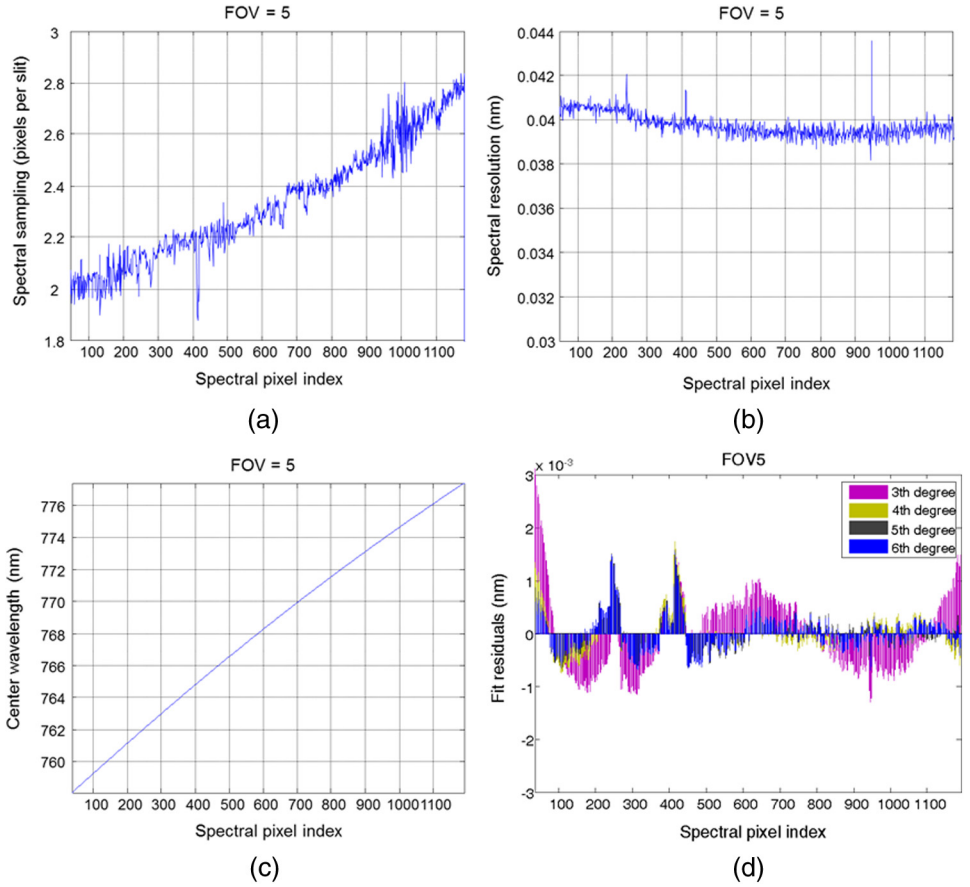

Fig. 17 Spectral sampling, spectral resolution and center wavelength as a function of spectral pixel index for the fifth spatial pixel of the 0.76-μm O_2 A-band (wavelength increasing with increasing spectral pixel index). (a) Spectral sampling over its wavelength range, spectral sampling increases with increasing wavelength. (b) Spectral resolution over its wavelength range, it is far more constant relative to spectral sampling. (c) Spectral dispersion relationships derived from the laser scans, the slope of the curve decreases with increasing wavelength (taking spectral pixel index 100, 600, and 1100, for example, slope 100 = 0.98, slope 600 = 0.87, slope 1100 = 0.73). (d) Residuals of polynomial fit to center wavelength of third order, fourth order, fifth order, and sixth order. The residual of third order is obviously large, the ones of fourth order, fifth order, and sixth order are almost the same.

sampled by 2 to 3 pixels in the direction of dispersion. Due to the anamorphic magnification of the slit at the different diffraction angles off the grating, spectral sampling varies with spectral pixel index, as shown in Fig. 17(a). Spectral resolution $\Delta\lambda$ can be expressed as

$$\Delta\lambda = n \cdot \delta\lambda, \tag{8}$$

where n is spectral sampling (the number of pixels per slit) and $\delta\lambda$ is spectral bandwidth of a single pixel. As shown in Fig. 17(b), spectral resolution $\Delta\lambda$ is far more constant relative to spectral sampling n over its wavelength range. From Eq. (8), $\delta\lambda$ decreases with increasing wavelength. Figure 17(c) shows the spectral dispersion relationships derived from the laser data for the fifth spatial pixel, which is consistent with this result. A slight curvature is visibly apparent, the slope decreases with increasing wavelength. So, $\delta\lambda$ of longer wavelengths is smaller, the signal received by spectral pixels with longer wavelengths is weaker. The intensity variation across wavelengths will be corrected by the laboratory radiometric calibration. Figure 17(d) shows residuals of polynomial fit to spectral dispersion of third order, fourth order, fifth order, and sixth order for the fifth spatial pixel. The residual of third order is obviously large, the ones of fourth order, fifth order, and sixth order are almost the same.

4.2 *On-Orbit Spectral Calibration*

The ILS and center wavelength of each spectral pixel were determined from diode-laser experiments. However, the parameters associated with the instrument laboratory spectral calibration may change due to the environment influences of vibration, distortion, and changed temperature during the period of launching and flight. Typically, shifts in center wavelengths are very likely to appear. As pointed out by most works,[32–35] small errors in spectral calibration parameters can introduce significant errors in the derived reflectance spectra. So, the onboard spectral calibration is indispensable. This section describes one method based on spectrum-matching technique to estimate the wavelength shift and then verifies the feasibility of this method. The onboard spectral calibration accuracy requirement is better than $\Delta\lambda/10$ ($\Delta\lambda$ is the spectral resolution).

A vibration testing on HRHS-GS with specialized equipment was conducted to simulate the mechanical shocks during the period of launching, which led to errors in the spectral parameters of the laser-based calibration. With the example of the 0.76-μm band, the deviation was identified and corrected by comparing solar spectrum recorded by HRHS-GS and the reference spectrum calculated by the line-by-line radiative transfer model (LBLRTM).

During thermal vacuum testing, the pointing mirror was fixed at one certain angle to direct sunlight into the HRHS-GS aperture. HRHS-GS acquired solar spectrum on 13:30 local time September 16, 2015. The solar spectrum measured by the 0.76-μm band of HRHS-GS is shown in Fig. 18.

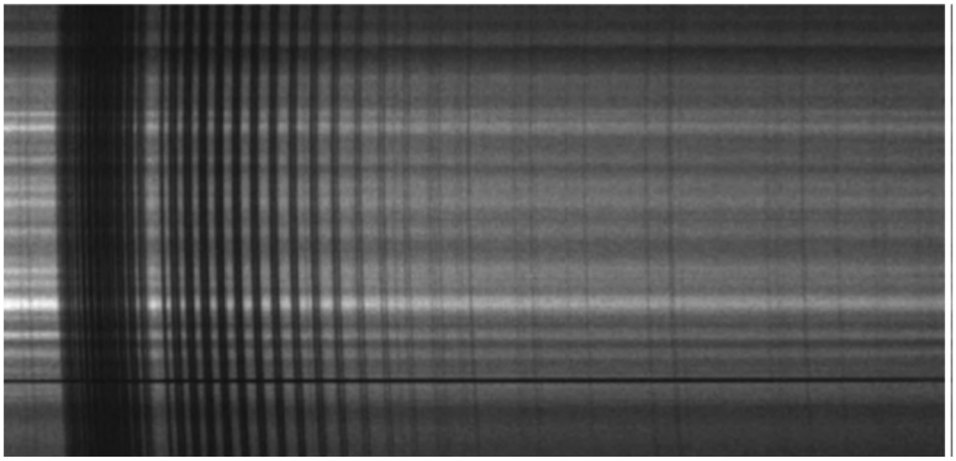

(a)

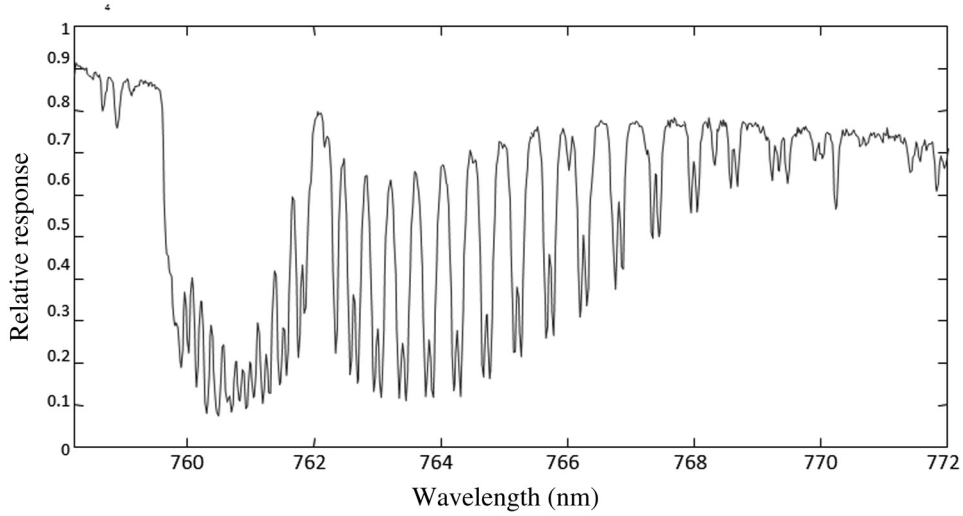

(b)

Fig. 18 Original image and measured solar spectrum. (a) Demonstration of original image collection. (b) Solar spectrum measured by the 0.76-μm O_2 A-band of HRHS-GS.

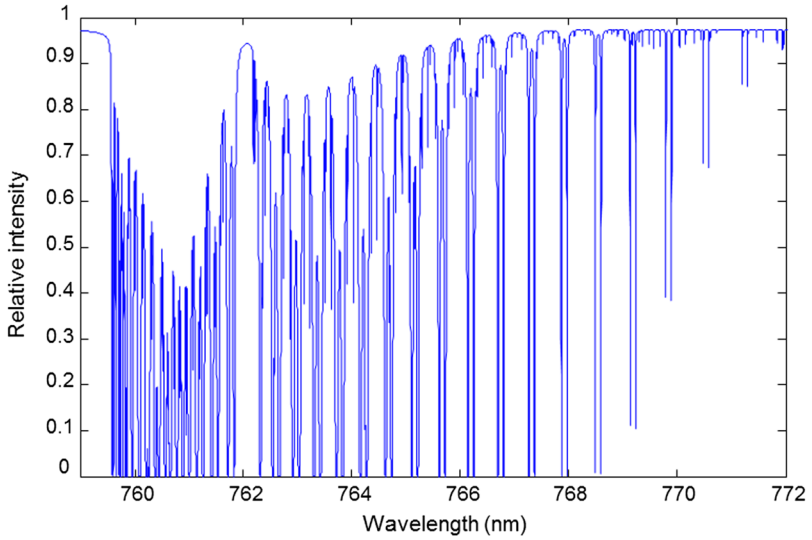

Fig. 19 The simulated spectrum calculated by LBLRTM with 0.035 cm^{-1} spectral resolution.

In order to validate the spectral calibration of HRHS-GS, a reference spectrum with much higher resolution was necessary. The atmospheric absorption lines were calculated by LBLRTM using HITRAN 2012 database.[36] The simulated spectrum was used as an ideal reference standard. Theoretically, the spectrum from LBLRTM could have very high spectral resolution; here, we set the spectral resolution at 0.002 nm (0.035 cm^{-1}), which is ~20 times higher than the spectral resolution of the 0.76-μm band of HRHS-GS. The simulated spectrum from LBLRTM is shown in Fig. 19.

In order to compare simultaneously the observed solar spectrum and the simulated reference spectrum calculated by LBLRTM, the high resolution simulated spectrum was convolved with the ILS of each spectral pixel of HRHS-GS to create a synthetic HRHS-GS-like spectrum at the 0.04-nm resolution. The measured spectrum and the simulated spectrum were normalized based on the maximum value. Figure 20 illustrates the comparison between the two spectra. The comparison showed that the spectral features and relative absorption depth of the two spectra had good consistency. However, there is corresponding deviation at the spectrum position.[37,38]

Through spectrum-matching technique the wavelength shift was estimated. Taking the results of the laboratory calibration as the initial solution, a Gauss–Newton iteration approach was used to perform the actual optimization. The optimization goal was to minimize root mean square, defined as the difference between the measured spectrum and the simulated spectrum derived

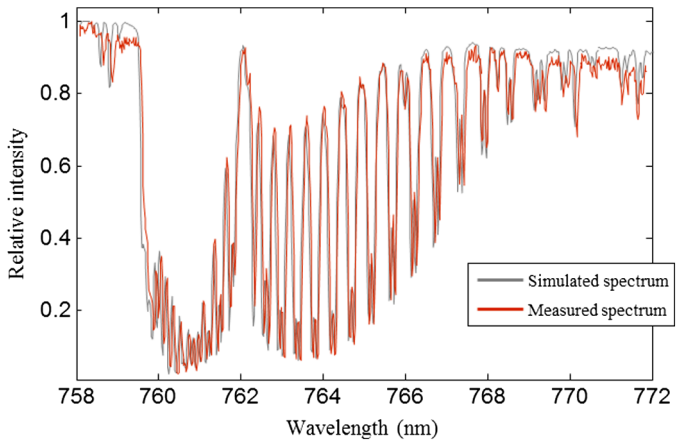

Fig. 20 Comparison between synthetic HRHS-GS-like spectrum (black) and actual atmospheric spectrum measured by HRHS-GS (red).

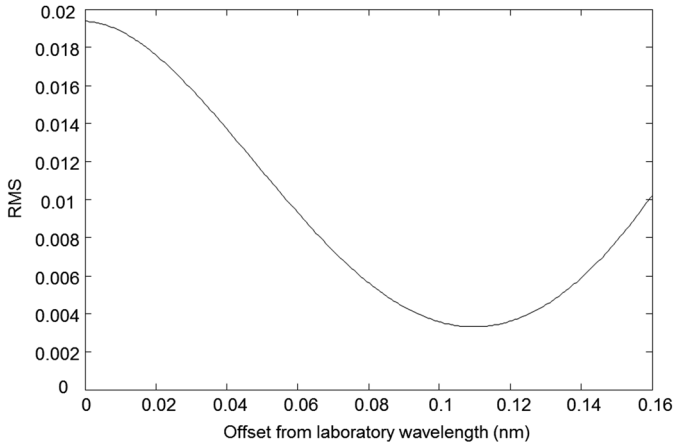

Fig. 21 The standard deviation between the measured spectrum and the simulated spectrum as a function of wavelength shift.

from HITRAN database. Figure 21 shows the standard deviation between the measured and simulated spectra as a function of wavelength shift. A minimum occurs at a wavelength shift of 0.11 nm. The measured spectrum was shifted to the left (short wavelength direction) by 0.11 nm. Figure 22 shows agreement between the measured HRHS-GS spectrum and simulated HRHS-GS-like spectrum after wavelength adjustment based on spectrum matching. The deviation between the absorption peaks of the two spectra was <0.003 nm, satisfying the onboard spectral calibration accuracy requirement of better than $\Delta\lambda/10$. Figures 20–22 demonstrate that, through the spectrum-matching technology, it is possible to estimate the wavelength shift for HRHS-GS in the on-orbit environment.

It should be noted that HRHS-GS had not been calibrated radiometrically. There was an intensity variation between the measured and the simulated spectra, resulting in larger standard

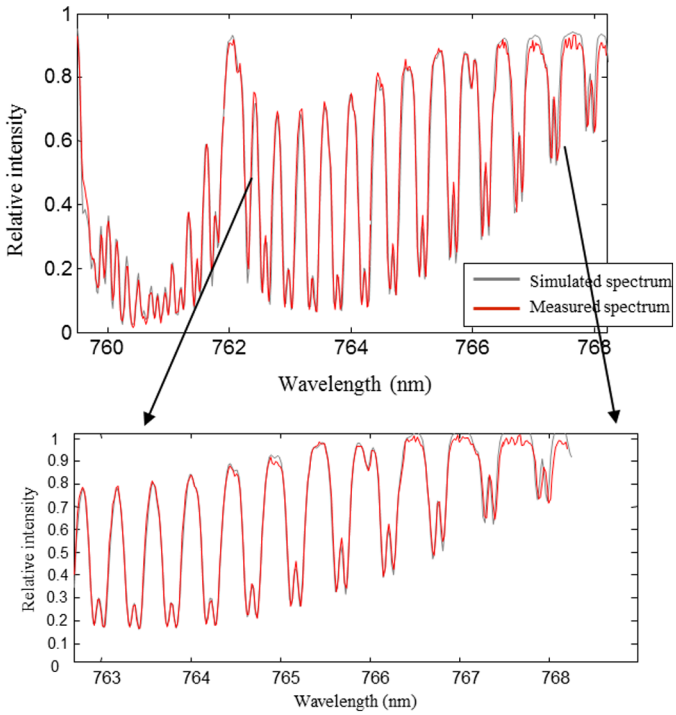

Fig. 22 Comparison between synthetic HRHS-GS-like spectrum (black) and actual atmospheric spectrum measured by HRHS-GS (red) after wavelength adjustment based on spectrum matching.

deviation between the two spectra. As noted above, $\delta\lambda$(spectral bandwidth of single pixel) decreases with increasing wavelength, $\delta\lambda$ of the long wavelength is small, the signal received by the long-wavelength pixels is weak. So, the intensity variation is more obvious at long-wavelength band, as shown in Fig. 22. Here, we introduce one onboard spectral calibration method and verify the feasibility of this method. In subsequent experiments, more accurate calibration results will be given.

5 Conclusions

This paper has introduced the Tan-Sat, which is the first Chinese satellite to measure the global distributions of CO_2 and O_2 from space. Tan-Sat carries two instruments: HRHS-GS and CAPI. HRHS-GS, the main payload of Tan-Sat, has three spectral bands, which cover narrow spectral ranges in the VNIR and SWIR. The main characteristics and the optical design of HRSR-GS were described. Three spectral bands share one common fore optics and adopt individual detectors according to different spectral ranges. In glint mode, the theoretical ocean reflectivity of TM and TE polarization was compared. The instrument polarization axis was perpendicular to the polarization state of reflected light, resulting in too little incident signal of the instrument over the ocean near the Brewster angle. Tan-Sat would be rotated 45 deg around the telescope optical axis for glint observations. The spectral calibration was described, ILS profiles and spectral dispersion were determined through the laser-based calibration. One on-orbit spectral calibration method based on spectrum matching was introduced. By comparing measured solar spectrum and simulated spectrum from HITRAN data sheet, wavelength shift was estimated and corrected. Because the radiometric calibration had not been finished, the standard deviation between two spectra was larger, in subsequent experiments, more accurate calibration results will be given.

According to the schedule, the laboratory spectral calibration and radiometric calibration of HRHS-GS will be finished before March 2016. Environment tests of Tan-Sat with HRHS-GS and CAPI will be implemented from March 2016 to June 2016. Tan-Sat is scheduled to be launched in July 2016.

Acknowledgments

The authors would like to thank every member of Carbon Observing Satellite science team, their contribution and kind support was necessary for this paper. This research was supported by the National High Technology Research and Development Program of China (Grant No. 2011AA12A102).

References

1. National Research Council, *Advancing the Science of Climate Change (2010)*, National Research Council, National Academies Press, Washington, DC (2010).
2. A. Kuze et al., "The instrumentation and the BBM test results of thermal and near infrared sensor for carbon observation (TANSO) on GOSAT," *Proc. SPIE* **6297**, 62970K (2006).
3. R. R. Basilio, H. R. Pollock, and S. L. Hunyadi-Lay, "OCO-2 (orbiting carbon observatory-2) mission operations planning and initial operations experiences," *Proc. SPIE* **9241**, 924105 (2014).
4. "Outline of the National Program for Long-and Medium-Term Scientific and Technological Development," 2006 www.most.gov.cn/yw/200602/t20060209_28602.htm
5. "China'S National Climate Change Programme," 2007 www.ccchina.gov.cn/WebSite/CCChina/UpFile/File188.pdf.
6. Y Liu et al., "Chinese carbon dioxide satellite (TanSat) status and plans," in *Proc. of American Geophysical Union 2012 Fall Meeting*, American Geophysical Union (2012).
7. J. Zhang, J. Shao, and C. Yan, "Cloud and aerosol polarimetric imager," *Proc. SPIE* **9142**, 91420X (2014).
8. J. Zhang et al., "Optical remote sensor for cloud and aerosol from space: past, present and future," *Chin. Opt.* **8**(5), 679–698 (2015).

9. L. Guanter et al., "Retrieval and global assessment of terrestrial chlorophyll fluorescence from GOSAT space measurements," *Remote Sens. Environ.* **121**, 236–251 (2012).
10. E. Karimi et al., "Generating optical orbital angular momentum at visible wavelengths using a plasmonic metasurface," *Light: Sci. Appl.* **3** (2014).
11. L. Maria Laurenza et al., "Comparison of column-averaged volume mixing ratios of carbon dioxide retrieved from IASI/METOP-A using KLIMA algorithm and TANSO-FTS/GOSAT level 2 products," *IEEE J. Sel. Top. Appl. Earth Obs. Remote Sens.* **7**(2), 389–398 (2014).
12. K. Shiomi et al., "GOSAT level 1 processing and in-orbit calibration plan," *Proc. SPIE* **7106**, 71060O (2008).
13. D. Crisp, C. E. Miller, and P. L. DeCola, "NASA Orbiting Carbon Observatory: measuring the column averaged carbon dioxide mole fraction from space," *J. Appl. Rem. Sens.* **2**(1), 1–14 (2008).
14. Y. Liu, D. X. Yang, and Z. N. Cai, "A retrieval algorithm for TanSat X_{CO2} observation: retrieval experiments using GOSAT data," *Chin. Sci. Bull.* **58**(13), 1520–1523 (2013).
15. Z. N. Cai, Y. Liu, and D. X. Yang, "Analysis of X_{CO2} retrieval sensitivity using simulated Chinese carbon satellite (TanSat) measurements," *Sci. China Earth Sci.* **57**(8), 1919–1928 (2014).
16. Y. Liu, Z. N. Cai, and D. X. Yang, "Optimization of the instrument configuration for TanSat CO_2 spectrometer," *Chin. Sci. Bull.* **58**(27), 2787–2789 (2013).
17. Y. Zheng and Z. Gao, "Optical system design of CO_2 sounder," *Opt. Precision Eng.* **20**(12), 2645–2653 (2012).
18. R. Haring et al., "The Orbiting Carbon Observatory (OCO) instrument optical design," *Proc. SPIE* **5523**, 51–62 (2004).
19. Y. Zhang, H. Yang, and C. Kong, "Spectral imaging system on laser scanning confocal microscopy," *Opt. Precision Eng.* **22**(6), 1446–1453 (2014).
20. Y. Bai et al., "Design of infrared optical system with super-long focal length and dual field-of-view," *Chin. Opt.* **7**(4), 631–637 (2014).
21. Z. Gao, "Design of hyperspectral imager equivalent focal plane assembling module," *Chin. Opt.* **7**(4), 644–650 (2014).
22. P. Girshovitz and N. T. Shaked, "Doubling the field of view in off-axis low-coherence interferometric imaging," *Light: Sci. Appl.* **3** (2014).
23. E2V Datasheet for 55–30.
24. Technical data package for Neptune SW LSF detector.
25. D. Crisp, "Measuring atmospheric carbon dioxide from space with the orbiting carbon observatory-2 (OCO-2)," *Proc. SPIE* **9607**, 960702 (2015).
26. J. O. Day et al., "Preflight spectral calibration of the orbiting carbon observatory," *IEEE Trans. Geosci. Remote Sens.* **49**(7), 2793–2801 (2011).
27. F. Sakuma et al., "OCO/GOSAT preflight cross-calibration experiment," *IEEE Trans. Geosci. Remote Sens.* **48**(1), 585–599 (2010).
28. Q. Han et al., "High-frequency radiometric calibration for wide field-of-view sensor of GF-1 satellite," *Opt. Precision Eng.* **22**(6), 1707–1714 (2014).
29. H. Cao et al., "Cross-spectral calibration for monochromator and imaging spectrometer," *Opt. Precision Eng.* **22**(10), 2585–2591 (2014).
30. J. Shi, S. Fu, and W. Xie, "Error correction of spectral response characteristic of grating spectrometer," *Chin. Opt.* **7**(3), 483–490 (2014).
31. H. Zhang et al., "Spectral detection with high spectral resolution and high signal-to-noise ratio based on remote sensing monitoring," *Opt. Precision Eng.* **23**(10), 229–238 (2015).
32. T. Wang et al., "Improved methods for spectral calibration of on-orbit imaging spectrometers," *IEEE Trans. Geosci. Remote Sens.* **48**(11), 3924–3931 (2010).
33. R. O. Green, "On-orbit radiometric and spectral calibration characteristics of EO-1 Hyperion derived with an underflight of AVIRIS and in situ measurements at Salar de Arizaro, Argentina," *IEEE Trans. Geosci. Remote Sens.* **41**(6), 1194–1203 (2003).
34. B. C. Gao, M. J. Montes, and C. O. Davis, "A curve fitting technique to improve wavelength calibration of imaging spectrometer data," in *Proc. 11th Annu. JPL Airborne Earth Sci.*, Vol. **3-04**, pp. 99–105 (2002).

35. Y. Feng and Y. Xiang, "Mitigation of spectral mis-registration effects in imaging spectrometers via cubic spline interpolation," *Opt. Express* **16**(20), 15366–15374 (2008).
36. L. S. Rothman et al., "The HITRAN 2012 molecular spectroscopic database," *J. Quant. Spectrosc. Radiat. Transfer* **130**, 4–50 (2013).
37. M. Gao and Y. Zheng, "Validation method of single-channel optical system design of CO_2 detector," *Chin. Opt.* **52**(1), 945–955 (2014).
38. F. Kataoka et al., "TIR spectral radiance calibration of the GOSAT satellite borne TANSO-FTS with the aircraft-based S-HIS and the ground-based S-AERI at the Railroad Valley Desert Playa," *IEEE Trans. Geosci. Remote Sens.* **52**(1), 89–105 (2014).

Hang Zhang received his MS degree in optics from Jilin University, Changchun, China, in 2010. He is an assistant researcher at the Changchun Institute of Optics, Fine Mechanics and Physics, Chinese Academy of Sciences (CAS). And he is currently working toward his PhD degree at Jilin University. His research is focused mainly on hyperspectral imaging and spectral calibration of optical remote sensing instruments. He is a member of the Carbon Observing Satellite science team.

Chao Lin received his MS degree in mechanical engineering from Jilin University, Changchun, China, in 2009. He is an assistant researcher at the Changchun Institute of Optics, Fine Mechanics and Physics, Chinese Academy of Sciences (CAS). His research interests include mechanical design and calibration of hyperspectral imaging instruments.

Yuquan Zheng received his PhD degree in optical engineering from the Changchun Institute of Optics, Fine Mechanics and Physics, Chinese Academy of Sciences (CAS), Changchun, China, in 2000. He is a senior researcher of Carbon Observing Satellite science team. His research is focused mainly on hyperspectral imaging, design of optical systems, and spectral calibration.

Wenquan Wang received his PhD degree in physics from Jilin University, Changchun, China, in 2001, and then completed postdoctoral research at the Hong Kong University of Science and Technology, Hong Kong, in 2002. He is currently a professor of physics at Jilin University. His research is focused mainly on the properties of metal alloy.

Longfei Tian received his MS degree in spacecraft design from Northwestern Polytechnical University, Xi'an, China, in 2013. He is an assistant researcher at the Shanghai Engineering Center for Microsatellites (SECM). His research field is spacecraft design, especially the spacecraft reliability and safety.

Dongbin Liu received his BS degree in circuits and systems from Peking University, Beijing, China, and MS degree in optical engineering from the Changchun Institute of Optics, Fine Mechanics and Physics, Chinese Academy of Sciences (CAS), Changchun, China. He is a researcher of the Carbon Observing Satellite science team. His research concerns the electronic design of imaging systems.

Shuai Li is currently pursuing his PhD degree in optical engineering from the Changchun Institute of Optics, Fine Mechanics and Physics, Chinese Academy of Sciences (CAS), Changchun, China. His research concerns the spectral calibration of hyperspectral spectrometers.